Electronic Supplementary Information (ESI) for:

Photoinduced charge flow inside an iron

porphyrazine complex

Longteng Tang,[†] Liangdong Zhu,[†] Maraia E. Ener,[‡] Hongxin Gao,[§] Yanli Wang,[†]

John T. Groves,[§] Thomas G. Spiro,*[,‡] and Chong Fang*[,†]

[†]Department of Chemistry, Oregon State University, 153 Gilbert Hall, Corvallis, Oregon 97331,

United States

[‡]Department of Chemistry, University of Washington, Box 351700, Seattle, Washington 98195,

United States

[§]Department of Chemistry, Princeton University, Princeton, New Jersey 08544, United States

*To whom correspondence should be addressed. E-mails: spirot@uw.edu (T.G.S.);

Chong.Fang@oregonstate.edu (C.F.).

Table of Contents

<u>**ESI Text**</u>

Experimental Materials and Methods:

Synthesis, purification, and preparation of the [(PyPz)Fe^{II}(OH$_2$)$_2$]$^{4+}$[4Cl$^-$] sample (FePz). The

FePz compound was prepared as we have previously reported.[1] Pyridine-2,3-dicarboxylic acid

(668 mg, 4 mmol), ferrous chloride tetrahydrate (199 mg, 1 mmol), urea (961 mg, 16 mmol) and

ammonium heptamolybdate tetrahydrate (12 mg, 0.01 mmol) were added to an uncapped round

bottom flask and heated at 180 °C for 30 min. Upon cooling, the solid product mixture was washed

sequentially with water, acetone, and methanol on a glass fritted filter at room temperature. The

obtained crude iron-2,3-pyridinoporphyrazine was added to 7 mL DMSO containing 5.0 g methyl

p-toluenesulfonate, and the solution was heated at 70 °C for 24 h. The cooled reaction mixture was

added into 250 mL of chloroform, leading to the precipitation of FePz (tetra-*p*-toluenesulfonate

salt). This product was then filtered on a glass frit, washed with acetone, and dissolved in methanol.

Subsequently, excess ammonium hexafluorophosphate was added to the methanol solution,

precipitating the hexafluorophosphate salt. The obtained solid was filtered and washed with a

mixture of 50/50 (v/v) isopropanol/diethyl ether, then dissolved in acetone and filtered.

At this point, excess tetra-*n*-butylammonium bromide (TBA-Br) was added to the acetone

solution and the bromide salt precipitated. This purified salt was then isolated by filtration and

washed with excess acetone until no (C$_4$H$_9$)$_4$N$^+$ ion could be detected by ESI-MS. The dark green

to black solid, [Fe^{II}Pz]$^{4+}$[4Br$^-$], achieved an overall yield of 21%. The chloride salt,

[Fe^{II}Pz]$^{4+}$[4Cl$^-$], was also prepared following the same procedure with tetra-*n*-butylammonium

chloride (TBA-Cl) instead of TBA-Br. We have checked that the FePz chloride salt shows the

same UV/Visible absorption, pK_a, NMR, and redox behavior as the FePz bromide salt. ^{1}H NMR

(500 MHz, D$_2$O): δ (ppm) 10.36 (4H, m), 9.37 (4H, m), 8.56 (4H, m), 5.92 (12H, m). ESI-MS:

$C_{32}H_{25}FeN_{12}{}^{+}$, calculated 632.1591, found 632.1583. The concentrated sample stock solutions were prepared by dissolving FePz crystals in 10 mM sodium phosphate buffer, pH=3, at which condition the complex is stable over the course of days. For the UV/Visible and transient absorption measurements, small aliquots of FePz stock solution were added to 10 mM sodium phosphate buffer at the desired pH values (at 3, 7, 9, or 11) to achieve solution samples with a visible absorbance maximum of ~0.4 in a 2-mm-pathlength quartz cell.

Femtosecond transient absorption (fs-TA) measurements. For the fs-TA experiment at OSU (e.g., see Fig. 1B, Fig. S2 and S3 below), we used a 400 nm actinic pump as the photoexcitation pulse which was obtained by second harmonic generation (SHG) of the 35 fs, 800 nm fundamental laser pulse (from a Legend Elite-USP-1K-HE regenerative amplifier system, Coherent, Inc.), followed by temporal compression using a prism pair (Suprasil-1, CVI Melles Griot) to ~40 fs pulse duration.[2,3] The power was reduced to ~0.2 mW via a neutral density filter. The probe pulse is a broadband supercontinuum white light generated by focusing a portion of the 800 nm fundamental pulse onto deionized water housed in a 2-mm-thick quartz cell (1-Q-2, Starna Cells), followed by temporal compression using a chirped mirror pair (DCM-12, 400—700 nm, Laser Quantum, Inc.).[4,5] We also performed the fs-TA experiment using a 480 nm actinic pump (see Fig. S5 below) with a redshifted probe window to track the excited state absorption band above 700 nm (hence truncating the ground state bleaching band below 500 nm), with a setup that involves a home-built two-stage noncollinear optical parametric amplifier (NOPA) followed by temporal compression via a chirped mirror pair (DCM-12, 400—700 nm, Laser Quantum, Inc.).[6] The solution sample was housed in a 1 mm pathlength quartz cuvette with an absorbance maximum of ~0.4 at ca. 480 nm (measured by a Thermo Scientific Evolution 201 UV/Visible spectrometer).

For the TA studies at UW, ~50 fs laser pulses were generated by a Libra Ti:Sapphire laser amplifier system (Coherent, Inc.). Approximately 75% (3 W) of the Ti:Sapphire output was used to pump an OPerA Solo Optical Parametric Amplifier (Coherent, Inc.) to generate the tunable excitation pulses across the near-UV to visible region (e.g., 370, 480, 520, 580, and 660 nm in Fig. S1), while the remainder fundamental output (1 W) was reserved for visible probe generation. The excitation and probe beams were directed into a Helios TA spectrometer (Ultrafast Systems, Sarasota, FL), where the broadband, visible probe light was generated at a thin sapphire plate. Samples were contained in quartz cuvettes with 2 mm pathlength, equipped with a stir bar and open to air (no effort was made to exclude oxygen). The TA spectra were collected in random order at 300 log-spaced time delays over the interval of ca. 2 ps to 5 ns; the spectra at each time point were averaged over three experimental scans. Data were processed with the Surface Xplorer software (Ultrafast Systems), and plotted in Fig. S1B-F (see below) and fit to single exponential decays using the Matlab 2014b curve fitting software (MathWorks, Inc.).

Tunable FSRS methodology. Our wavelength-tunable FSRS experimental setup has been reported previously.[3,7] In brief, the fundamental output from a Ti:sapphire regenerative amplifier (Legend Elite-USP-1K-HE, Coherent, Inc.) is at ~800 nm center wavelength, 1 kHz repetition rate, ~35 femtosecond (fs) pulse duration, and 4 W average power. The tunable fs actinic pump (ca. 480 to 720 nm) is based on our homebuilt two-stage NOPA, followed by temporal compression using a prism pair (AFS-SF10, Thorlabs, Inc.). As for the 400 nm actinic pump (0.2 mW measured before the sample), SHG of the fundamental output in a thin BBO crystal is used with its power tuned by a neutral density filter in the beampath, followed by temporal compression using a prism pair (Suprasil-1, CVI Melles Griot). The picosecond (ps) narrowband Raman pump (same tunable

range from ~480 to 720 nm) is generated via a homebuilt three-NOPA setup (i.e., one provides the seed pulse in the fs domain and two achieve sequential amplification in the ps domain), a grating-slit-based spectral filter (converting the fs seed to ps seed), and a second harmonic bandwidth compressor based on opposite chirp cancellation.[7] The probe pulse is a supercontinuum white light (SCWL), generated by focusing a portion of the fundamental laser output pulse onto a 3-mm-thick sapphire plate, then compressed in the time domain via a prism pair (AFS-SF10, Thorlabs, Inc.). All the incident pulses were parallel-polarized at the sample position. The FePz aqueous buffer solution sample was contained in a 1-mm-pathlength quartz cuvette (1-Q-1, Starna Cells) with an OD≈1/mm at ca. 483 nm (see Fig. 1A) for the ground and excited-state FSRS measurements. For data presentation in Figure 2 (main text), the ground state spectrum (displayed at the bottom) is a difference spectrum[3,8] between the experimentally obtained solution and solvent (stimulated Raman gain) spectrum. The time-resolved excited state spectrum (displayed at the top) is a difference spectrum between the experimentally obtained excited state spectrum at each time delay (following the actinic pump) and the ground state spectrum.

Additional notes on the selection of actinic pump and Raman pump wavelengths for FSRS. Several experimental conditions other than the one reported in main text have been attempted to acquire the excited state (ES) Raman spectra of FePz in water but no ES Raman modes were clearly resolved for this novel metal-organic compound.[1] In particular, we used 400 nm actinic pump (as photoexcitation) with the 800 or 560 nm Raman pump to collect the time-resolved FSRS data in the electronic excited state. It became clear that the 400 nm pulse cannot pump the sample as efficiently as the 480 nm pulse because the ferrous complex absorption band in the visible region peaks at ~483 nm in pH=3 aqueous buffer solution (see Fig. 1A).[1] The pH-dependent UV/Visible

spectra of FePz (pH = 5.72–11.18) confirm the assignment of the 483 nm peak to the ferrous complex species, while the spectrophotometric titration reveals two pK_a values at 8.0 and 10.1 in association with the successive deprotonation of two axial water molecules.[1] Therefore, a direct excitation of this ~480 nm band ensures that we could observe and track the spectral response from the intended ferrous species. In addition, the 800 nm Raman pump cannot provide sufficient pre-resonance enhancement of the ES Raman signal because it is on the far edge of the excited state absorption (ESA) band (see Fig. 1B).[2,9]

　　With the 480 nm actinic pump that better populates the ES species of FePz, we employed the 700 and 720 nm Raman pump with both the Stokes and anti-Stokes FSRS to take advantage of the ESA band around 700 nm for resonance Raman enhancement.[9] Note that the Stokes and anti-Stokes Raman terminology has been used to refer to the FSRS experiments with redder and bluer Raman probe, respectively, with respect to the Raman pump. However, in the Stokes FSRS, we could not clearly resolve any high-frequency modes because the Raman probe around 800 nm has strong interference with the residual of the laser fundamental pulse (i.e., for SCWL generation).[10] In the anti-stokes FSRS experiment, the signal-to-noise ratio is also low because the more energetic probe photons are now strongly absorbed by the ground state species (see the prominent 633 nm absorption peak in Fig. 1A). Therefore, we selected the optimal experimental condition on the basis of Fig. 1 to be the 480 nm actinic pump, 554 nm Raman pump, and Stokes Raman probe on the lower energy side (main text). Recently, a number of other groups have also adopted similar FSRS techniques, aided by fs-TA spectroscopy and quantum calculations, to study a range of functional molecules and/or materials and broaden the appeal and impact of the powerful FSRS methodology and integrated characterization platform.[11-14] Additional characterization technique includes the tabletop M-edge X-ray absorption near-edge structure (XANES) spectroscopy that

could distinguish between the metal- and ligand-centered excited states, and an application on an Fe$^{(III)}$TPPCl complex tracked LMCT state that returns to ground state with ~1 ps time constant.[15]

In particular, for the transition-metal complex in our current work, the ~480 nm electronic band in Fig. 1A is likely an Fe^{II} → Pz charge transfer (MLCT) transition which generates the Fe^{III}Pz$^{(-)}$ species after photoexcitation (*vide infra*). In other words, instead of a direct π→π* transition of the ligand ring system, the electrons in the central-metal d orbitals are directly excited to the ligand π* orbitals upon interaction with the fs actinic pump pulse (see TOC Graphic for illustration). As the system moves out of the Franck-Condon region along the excited state multidimensional potential energy surface, a strong correlation between atomic motions and the electronic state evolution in the FePz complex could reflect the stimulated Raman modes being resonantly enhanced by transient electronic transition bands, while these characteristic motions move the molecule along the excited state potential into the intermediate d-d state (see Scheme 1, main text).[3,9,10] On a more fundamental level, this work elucidates an ultrafast interplay between the nuclei and electrons in a photoexcited molecular complex solvated by water molecules.

ESI Figures
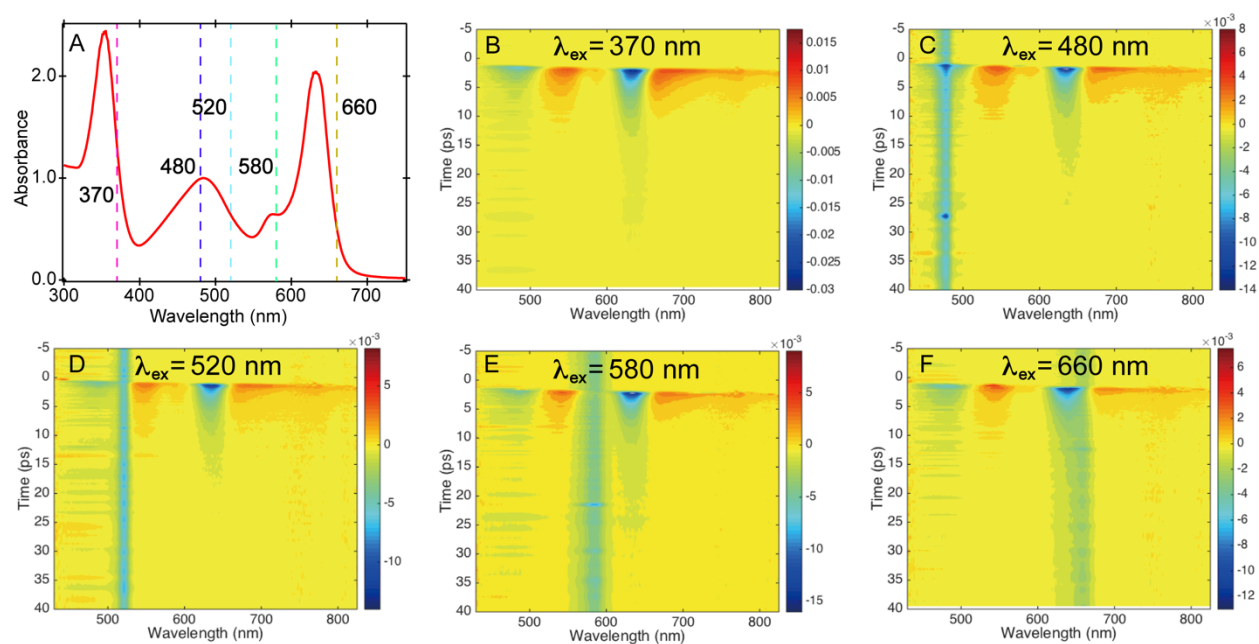
Fig. S1. Ground and excited state electronic spectra with different excitation wavelengths. (A) Steady-state electronic absorption spectrum of FePz in pH=3 aqueous buffer solution with 10 mM sodium phosphate. (B)–(F) The broad and overlapping transient electronic bands across the probe detection window from the near-UV to near-IR region with the pump wavelength of (B) 370 nm, (C) 480 nm, (D) 520 nm, (E) 580 nm, and (F) 660 nm. Prominent features include two ground-state bleaching bands (blue) at ~485 and 632 nm, and two excited-state absorption bands (red) at ~550 and 690 nm. All the experiments were performed at room temperature.

Notably, the time-resolved excited-state electronic spectrum and decay kinetics are unaffected by the excitation wavelength across a wide region (see vertical dashed lines in panel A). For instance, the bleach observed at ~633 nm is due to depletion of the ground-state ferrous species, which overlaps with the nascent excited-state ferric species (i.e., formally producing Fe(III)Pz$^-$). Although the ground-state ferric species absorb on the bluer side with higher intensity than the

ferrous species in this Q-band region,[1] we did not generate the ground-state ferric form in our TA and FSRS experiments (e.g., Figs. 1–4 in main text, and Figs. S1–S5 here). Therefore, the negative bleach peak is expected in the experimental TA spectra as confirmed by Fig. 1B and Fig. S1B-F.

In addition, previous work on the diaqua Fe(III) porphyrazine and Fe(II) porphyrazine at pH=2.2 buffer solution showed that the ~480 nm absorption band (see panel A above) largely disappears upon generating the Fe(III) complex from the Fe(II) complex electrochemically or by chemical oxidation, strongly suggesting the MLCT assignment of this band involving the contribution from the central metal Fe(II).[1] Further experimental corroboration for the band origin comes from the pH-dependent steady-state absorption spectra reported in literature,[1] which showed pronounced spectral changes of the FePz complex as the axial ligands (H_2O in this case, see Fig. S1A for a representative spectrum in pH=3 aqueous solution) are successively deprotonated. The titration was reversible and gives identical two pK_a values of ~8.0 and 10.1 (quoted in main text) within the pH range of 5 to 12. While the equatorial porphyrazine moiety remains the same, deprotonation occurs at the axial water ligand sites, which reduces the positive charge on the Fe(II) and lowers the MLCT energy, hence the observation of strong red-shifts in the ~480 nm absorption band.[1] These key observations substantiate the importance of this MLCT state and its high sensitivity to the metal-ligand interactions in the FePz complex.

Interestingly, the recovery of the ground-state bleaching band at 632 nm occurs with a ~4 ps time constant, while the other bands exhibit similar dynamics. Such a rapid deactivation of excited state species may indicate the ultrafast transition between adjacent electronic states (e.g., MLCT and metal-centered states)[16] and the coupled electron and structural motions that do not involve large-scale conformational change. In essence, the pump-wavelength-independent TA signal pattern in Fig. S1B-F strongly indicates an ultrafast conversion from the initially accessed excited

S10

state manifold (with the mixed metal-ligand transitions) to the metal-centered d-d state (for an effective surface crossing from the excited state to ground state). Further structural dynamics insights can thus be obtained by the 480 nm photoexcited FSRS modes that track the MLCT-to-d-d conversion (see Fig. 2 in main text and Fig. S4 below).
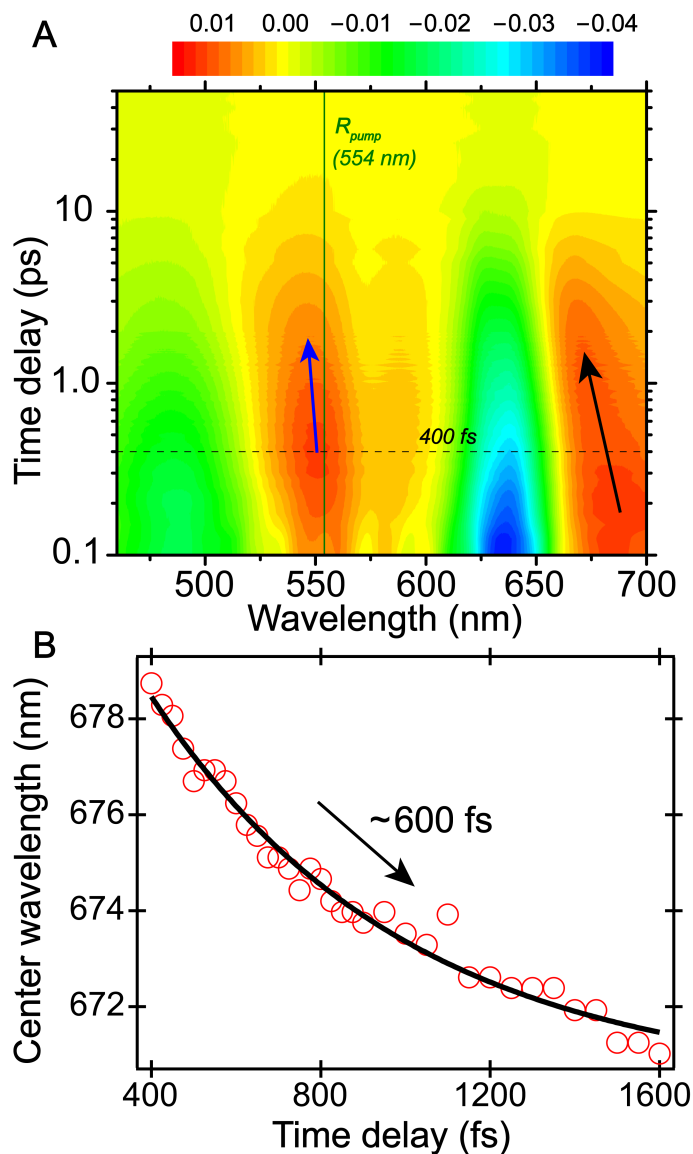
Fig. S2. Transient absorption spectra of FePz in pH=3 aqueous buffer solution. (A) Contour plot of the transient absorption spectra of FePz after 400 nm photoexcitation from 100 fs to 50 ps. The ESA band above 660 nm exhibits a clear blueshift (black arrow), while the later-peaked ESA band at ~550 nm also shows a blueshift (blue arrow). The Raman pump at 554 nm (vertical green line, also see Fig. 1 in main text) was used in the excited state FSRS experiments. The time delay of 400 fs is highlighted by the black dashed line. (B) The redder ESA band center wavelength (red circles) blueshift dynamics can be fit with a single exponential time constant of ~600 fs (black).

The observed ~600 fs time constant is longer than the ~160 fs retrived from the excited-state Raman mode frequency shift (Fig. 3A) due to different dependence of electronic and vibrational bands on the excited state energy relaxation pathways.[5,10] In contrast to the normal-mode-dependent dynamics that probe local environment at chemical bond level, the electronic peak wavelength evolution reports on the overall potential energy surface (PES) from one electronic state to the other which could involve multiple vibrational motions of different parts of the molecule and vibrational relaxtion after reaching a transient electronic state.[10,13] Interestingly, the bluer ESA band at ~550 nm reaches peak maximum at ~400 fs (see Fig. S2A, and Fig. S3 for the least-squares fit) and then exhibits a clear blueshift of its center wavelength, which differs from the redder ESA band at ~680 nm that peaks at ~200 fs and displays a continuous blueshift of center wavelength. This comparison implies that both ESA bands involve spectral contributions from multiple transient electronic states of FePz in water, while the bluer and redder ESA band is more sensitive to the lower-lying d-d state and higher-lying MLCT state, respectively (see Scheme 1). Further evidence can be obtained from the ESA band dynamics plot in Fig. S3 and S5 below, though an exact match between the TA intensity dynamics time constants is not expected at various probe wavelengths (e.g., 680 and 720 nm) due to spectral overlap with adjacent electronic states.

The apparent ESA peak blueshift on the fs to ps timescale before the peak diminishes after ~10 ps is consistent with the initially populated MLCT state undergoing a highly efficient intersystem crossing into a lower-lying d-d state (intermediate spin hence close in energy to the MLCT state), and further relaxtion within that d-d state before returning to the electronic ground state. We note that the 400 nm excitation generates a TA profile similar to those in Fig. S1B-F (the signal magnitude closely matching that in Fig. S1B), corroborated by the broad absorption profile of FePz in aqueous solution across the visible region (Fig. S1A).
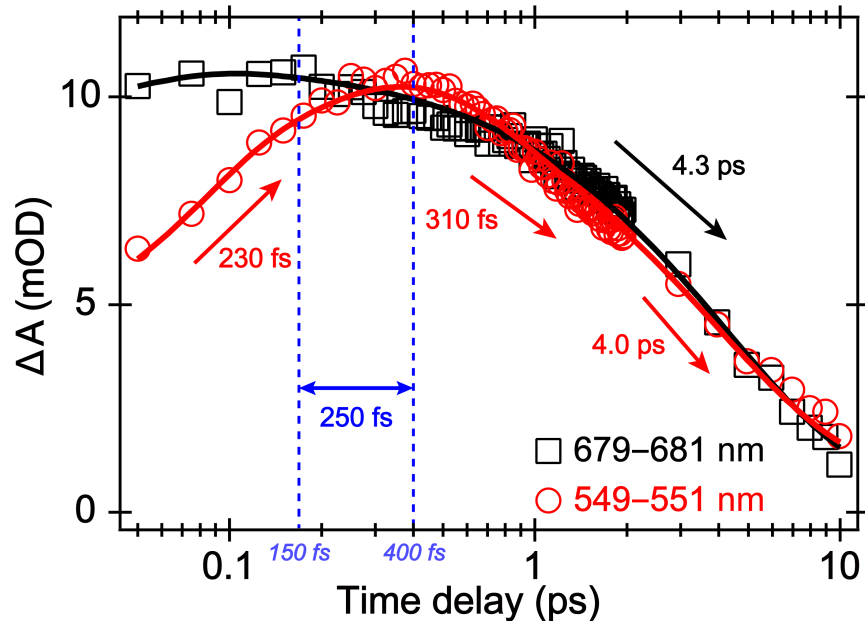
Fig. S3. Probe-dependent transient absorption (TA) dynamics of FePz in pH=3 aqueous buffer solution after 400 nm excitation. The ESA band dynamics above 660 nm and below 570 nm are represented by the integrated signal intensity from 679–681 nm (black squares) and 549–551 nm (red circles), respectively. The multi-exponential fits of time-resolved data are shown in the color-coded solid curves with the associated time constants listed. Temporal separation between the two ESA peaks is highlighted by the vertical blue dashed lines and the double-arrowed blue line.

Notably, the ESA band dynamics at ~550 nm can be least-squares fitted with three exponentials starting from the same time zero with one rise (~230 fs) and two decay components of ~310 fs (61% amplitude weight) and 4.0 ps (39% weight). For dynamics of the ~680 nm ESA band, it rises within the experimental cross-correlation time (<100 fs) and decays with a single exponential time constant of ~4.3 ps. The delayed maximum of the ~550 nm ESA band at ~400 fs indicates an ultrafast transition from the initially populated electronic state (likely responsible for the ~680 nm ESA band with MLCT character) to an adjacent, lower-lying d-d state (Scheme 1). This unique reaction scheme is further corroborated by the excited-state FSRS mode dynamics (see Fig. S5).
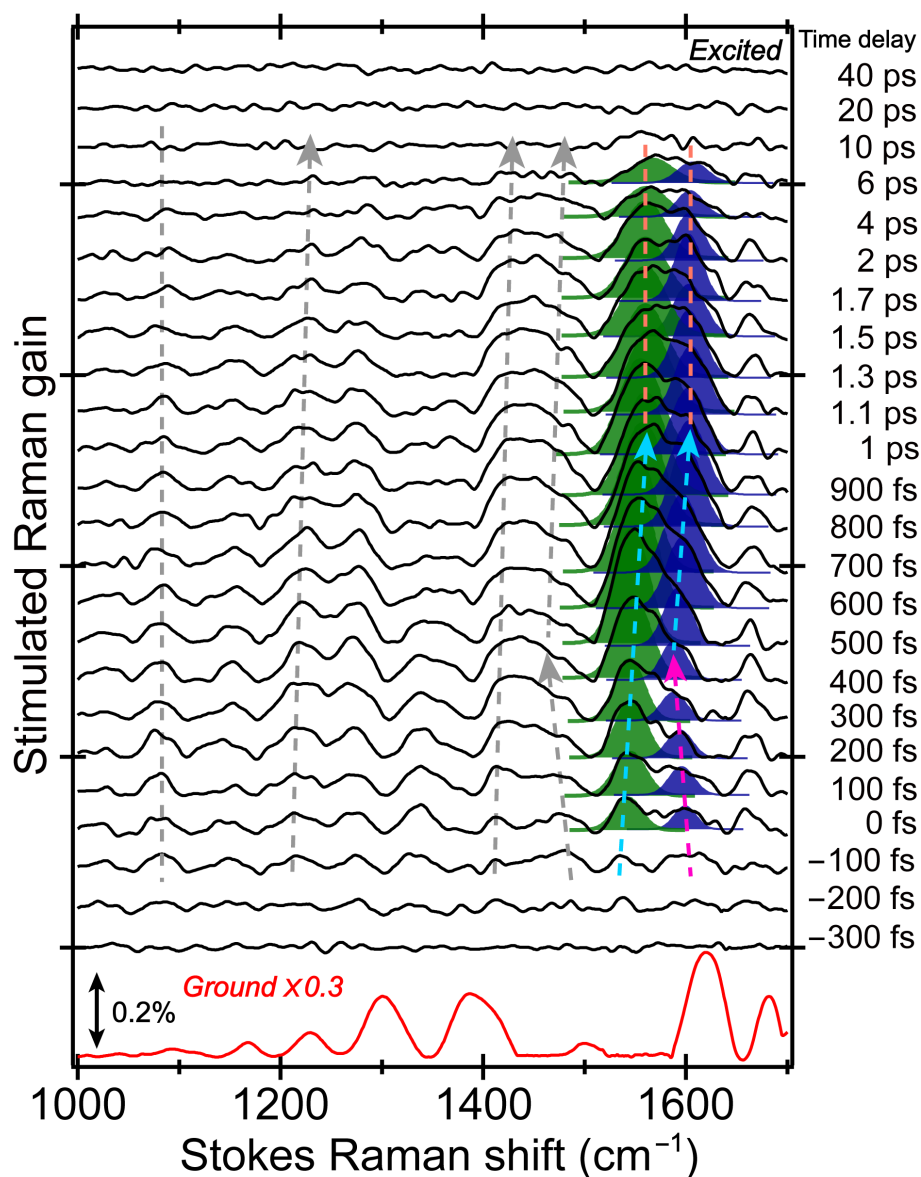
Fig. S4. Time-resolved excited state (ES) FSRS spectra (black) of FePz in pH=3 aqueous buffer solution from −300 fs to 40 ps after 480 nm photoexcitation. The Raman pump is tuned to 554 nm. The scaled ground state FSRS spectrum (red) is plotted below. The stimulated Raman gain of 0.2% is depicted by the double-arrowed vertical line. Cyan and magenta dashed arrows track frequency shifts in the 1500—1650 cm⁻¹ region. Gray arrow shows smaller frequency shifts that are present for some other excited state Raman modes, while the gray and orange vertical lines highlight the mostly frequency-stagnant modes (i.e., the observed center frequency shifts with various

S15

magnitudes and/or directions are characteristic of each vibrational mode). Two prominent Raman marker bands in S_1 from multi-gaussian least-squares fitting are shown above 1500 cm^{-1} to provide convincing experimental evidence for the reported frequency dynamics (see Fig. 3A, main text).

Vibrational peak frequency dynamics in time-resolved FSRS reveal important information about the excited state relaxation pathways.[10,17] The Raman mode frequency shifts are apparent from the time-stacked transient spectra in the electronic excited state after actinic photoexcitation, while the observed Raman modes assume largely absorptive lineshapes. Note that the difference spectra in Fig. 2 and Fig. S4 above are ground-state-subtracted, and the photoexcited population is typically less than 10% of the original ground state population.[8,10] The intensity of these transient Raman modes largely decays to zero at about 10 ps, corroborating the ground state recovery with the ~4 ps time constant (Fig. S1 and S3, also see Scheme 1 in main text). Interestingly, the dynamic up-shift of the ~1595 cm^{-1} mode on the few ps timescale (Fig. 3A) is toward the ground state value of ~1620 cm^{-1} (Fig. 2 bottom). The initial intensity and frequency dynamics upon electronic excitation are better shown in Fig. 2 (main text, 2D contour plot).

In addition, for FePz in pH = 9 and 11 aqueous buffer solution using a 600 nm Raman pump, the ground state Raman mode frequencies for both the inner and outer ligand ring modes (Fig. 3B and C) exhibit a redshift of ~10 cm^{-1}, which suggest that more electrons shift from the central metal to the π^* orbitals of the ligand ring so the double-bond order decreases to some extent. The axial water ligand now becomes the hydroxide, which causes a substantial shift in orbital configuration and likely pushes more electron via the overlapped low-spin Fe$^{(II)}$ d(π) orbital and Pz ring π^* orbital to the ligand ring system (see TOC Graphic for illustration, initial step 1). Once again, FSRS data provide experimental evidence for the MLCT band in the Fe(II)Pz complex.
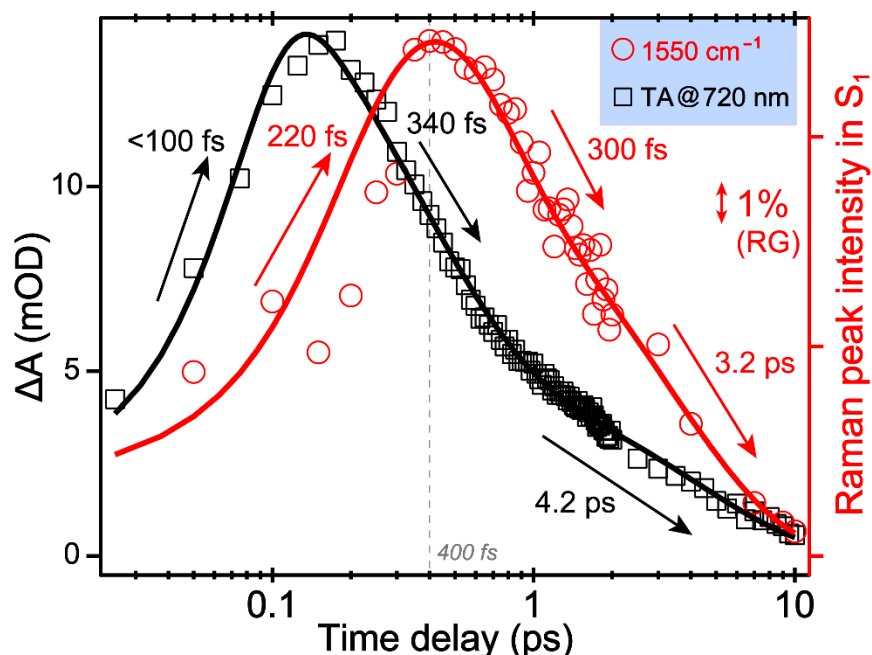
Fig. S5. Comparative plot between the fs electronic and vibrational dynamics of FePz in pH=3 aqueous solution after 480 nm photoexcitation. The TA dynamics at 720 nm probe (black squares, corresponding to the excited state absorption band; left axis) exhibit notable differences from the FSRS intensity dynamics of the excited state 1550 cm^{-1} mode (red circles; right axis) upon 480 nm photoexcitation. The least-squares fits in color-coded solid traces are overlaid with data points. The time axis is on a logarithmic scale. The double-arrowed vertical line indicates a stimulated Raman gain (RG) of 1%. The integrated peak intensity of the Gaussian-fit Raman band is shown.

The initial metal-to-ligand charge transfer (MLCT, as described in main text) and rapid intersystem crossing (ISC from MLCT to a lower-lying d-d state, see Scheme 1) can affect the polarizability of certain vibrational motions, thus leading to a ~220 fs rise and 300 fs decay of the 1550 cm^{-1} ligand-ring-stretching marker band. In contrast, the TA signal rises within the corss-correlation time (<100 fs), followed by a biexponential decay with 340 fs (69% amplitude weight) and 4.2 ps (31% amplitude weight) time constants. The 340 fs component is likely due to a mixture of structural relaxation within the MLCT state (via intramolecular vibrational energy redistribution,

or IVR) and the subsequent ISC to the d-d state, as the associated vibrational frequency dynamics exhibit characteristic time constants of ~150 fs and 160 fs, respectively (Fig. 3A, Scheme 1 in main text). Due to direct excitation into the MLCT state not a ligand π-π* excited state, the ligand π orbitals are filled and do not participate in the subsequent CT processes as described (main text).

In the excited state vibrational domain, the 1550 cm^{-1} mode intensity exhibits a biexponential decay with 300 fs (45% amplitude weight) and 3.2 ps (55% amplitude weight) time constants which largely match the TA decay time constants. From the least-squares fit, the time zero for the ~220 fs rise component is −30 fs whereas the time zero for the ~300 fs and 3.2 ps decay components is 400 fs, highly consistent with the "turning point" in the frequency shift dynamics of two high-frequency marker bands of FePz (see Fig. 3A) as well as the delayed peak maximum of the ~550 nm ESA band (see Fig. S2A and S3). We remark that the signal-to-noise ratio of the observed Raman peak is governed by the resonance condition as the molecular system navigates the excited-state potential energy landscape, which leads to the apparent dynamics of some vibrational marker bands (e.g., the 1550 cm^{-1} mode in Fig. S5 above) with its peak intensity maximum shifted to a few hundred of femtoseconds after the time zero of photoexcitation. In consequence, the least-squares fitting procedure[3,6,13] that convolutes a model rise and decay function with an instrument response function (i.e., the cross-correlation time was measured to be below 100 fs in our work) needs to be expanded to take into consideration the dynamic resonance enhancement of excited-state Raman peak intensity,[9,10] which is a non-trivial task. In order to retrieve a more realistic percentage of amplitiude weight of the two decay components (i.e., ~300 fs and 3.2 ps processes for the red trace above), we shifted the fitting time zero to 400 fs to be in accord with Fig. 3A.

After ~400 fs, further blueshift of the ESA band center wavelength reflects vibrational cooling within the nascent d-d state before returning to S_0. Given the overall blueshift time constant of

~600 fs for the ~680 nm ESA band (Fig. S2B) and the ~300 fs time constant observed here for the excited-state 1550 cm^{-1} mode intensity, we estimate the vibrational relaxation time within the lower-lying d-d state to be ~300 fs as denoted in Scheme 1. This value is corroborated by the ~550 nm ESA band intensity dynamics (Fig. S3) showing a notable 310 fs decay component, which is considered to be highly sensitive to the d-d state relaxation. The excited d-d state would rapidly convert to the electronic ground state (i.e., a ground state Pz ring system with an excited iron d-electron configuration), and the 3–4 ps decay of the ESA band as well as FSRS mode intensity likely involves IVR processes in the ground state (see Fig. 4 and main text).[16]

Notably, the concomitant decay of the ESA band at 720 nm and rise of the 1550 cm^{-1} mode (see Fig. 3B for the associated nuclear motion) indidates that (1) the excited-state 1550 cm^{-1} mode is conserved from the MLCT to the d-d state, (2) the optimal resonance Raman effect is achieved at the lower portion of the MLCT state but not with the d-d state, also corroborated by the ESA band center wavelength blueshift dynamics in Fig. S2A, (3) the time constants from fitting the mode intensity dynamics are typically larger than those from the frequency dynamics because multiple factors contribute to the apparent Raman mode intensity,[10] and (4) direct comparison of the probe-dependent electronic dynamics and vibrational mode-dependent dynamics provides a useful way to dissect the excited state relaxation as the system navigates the multidimensional potential energy surface with dynamic resonance conditions and associated Raman enhancement factors for the observed Raman modes in the time-resolved excited state FSRS.[3,9]

These new spectroscopic results substantiate the key role played by ultrafast CT within the photoexcited FePz system on the fs to ps timescale, and the sequential nature of the relaxation and transition between two spectrally distinguishable electronic states (Scheme 1). The associated structural motions have been vividly captured to play a functional role of the FePz photochemistry.

Although these results rule out photocatalysis by unmodified FePz, we report our research motivation and strategies for extending the excited state lifetime, in hopes that it will inspire further work on this interesting complex and its functional derivatives.

Last but not least, we note that the focus of this work is not to study other metal-organic complexes that already have a long-lived MLCT or LMCT state,[18,19] but to elucidate the photophysical and photochemical properties of this novel iron porphyrazine (FePz) complex and gain insights into ways to extend its excited state lifetime. Since iron is by mass the most common element on earth and second most abundant metal (after aluminum), which are inexpensive and readily available, mechanistic studies on the iron complex have general implications for a variety of applications across disciplines. For instance, "making iron glow"[20] or acquiring photocatalytic properties (see comparisons with the nickel complex in main text, although the long-lived state in the NiPc is LMCT,[18] not MLCT, so the chemistry that might be catalyzed would be reductive instead of oxidative) have been a research goal of many scientists and engineers.

ESI Tables

Table S1. Excited state Raman mode assignments for FePz in acidic aqueous solution

Exp. Freq. (cm^{-1})^a	Cal. Freq. (cm^{-1})^b	Vibrational Mode Assignment (major)
1083^c	1086	Inner ring asymmetric breathing and outer ring-H rocking
1222^c	1213	Inner ring breathing, outer ring in-plane deformation with ring-H scissoring
1272^c	1276	Inner and outer ring in-plane deformation and outer ring H-rocking
1337^d	1349	Outer ring in-plane asymmetric deformation, C=N stretching with ring H-rocking
1425^c	1420	Outer ring-H rocking with small-scale ring in-plane deformation
1467^c	1468	Outer ring-H rocking with small-scale inner ring in-plane deformation
1550^e	1547 / 1545^f	Inner ring C=N stretching with small-scale outer ring-H rocking
1595^e	1584 / 1579^f	Outer ring C=C and C=N stretching with some outer ring-H scissoring

^{a} The observed excited state (S$_1$) Raman mode frequencies of the FePz molecule in aqueous solution (pH=3) as retrieved from the ES-FSRS data in Fig. 2 (see main text) and Fig. S4.

^{b} The ground state Raman mode frequencies are calculated in the Gaussian 09 software[21] by density functional theory (DFT) at the RB3LYP level with 6-31G basis sets of the geometrically optimized [(PyPz)Fe^{II}(OH$_2$)$_2$]$^{4+}$ structure in aqueous solution (see Fig. 1A inset and Fig. 3B, C for the chemical structure). Bulk solvent of water is treated using the integral equation formalism variant polarizable continuum model (IEFPCM). The calculated vibrational normal mode frequencies are scaled by a factor of 0.96, typical for this level of theory.[22] The excited state vibrational frequencies can be retrieved from time-dependent DFT (TD-DFT) calculations using the same basis sets, but

due to the output in IR (i.e., not Raman) peak intensities associated with an optimized structure in S_1, we did not list those frequencies to compare with the observed Raman mode frequencies in S_1. However, characteristic atomic motions associated with the vibrational normal modes are similar in frequencies going from S_0 to S_1, corroborating the major mode composition and assignment listed in Table S1. Moreover, different theory level (e.g., PBE0) with the same 6-31G basis sets or hybrid basis sets lead to similar vibrational frequencies with significant polarizabilities, which substantiates the robustness of Raman mode assignment using DFT calculations as they are less dependent on the choice of exchange-correlation functional at a reasonable computational cost.[23,24]

[c] These Raman modes exhibit various frequency dynamics. In particular, the 1083 cm^{-1} mode shows no obvious frequency shift in ES-FSRS (see Fig. 2 and Fig. S4). The 1222, 1272, and 1425 cm^{-1} modes show a slight blueshift by ~8 cm^{-1} or less, while the ~1467 cm^{-1} mode shows a redshift then blueshift. Such vibrational-mode-dependent frequency dynamics are expected for the multi-dimensional photochemical reaction coordinates found in functional molecules in solution.[10,13]

[d] This mode can be fit with a peak doublet with distinct intensity dynamics (i.e., fastest decay) among all the observed S_1 Raman modes. It suggests that the outer ring asymmetric deformation is highly sensitive to the initial MLCT relaxation (Scheme 1), which completes within ~400 fs (see Fig. 3A for vibrational frequency dynamics, and Fig. S2 for transient electronic dynamics).

[e] These two highly specific and localized (with respect to the inner or outer ligand ring system) Raman bands are explicitly assigned and discussed in main text (Fig. 3B and C). They exhibit the highest intensities and most significant frequency shifts on the fs to ps timescale (Fig. 2 and 3A).

[f] These values from TD-DFT calculations using hybrid basis sets (see Table S2 below) exhibit a small redshift (≤5 cm^{-1}) from the DFT calculation results (using the same frequency scaling factor), confirming the robustness of vibrational mode assignment for these Raman marker bands.[10,13]

Table S2. The charge of Fe in the ground and excited states by DFT and TD-DFT calculations with various basis sets

Basis Sets	Mulliken Charge		NBO Charge	
Genecp (SDD for Fe, and 6-31G(d,p) for C, H, O, N)	GS	0.692	GS	0.385
	ES	0.713	ES	0.523
Genecp (LANL2DZ for Fe, and 6-31G(d,p) for C, H, O, N)	GS	0.5		
	ES	0.555		
6-31G	GS	1.448		
	ES	1.556		

GS: Ground state.　　ES: Excited state.

The Mulliken and NBO charges of Fe in the ground and excited states are calculated by the DFT method with RB3LYP functional and different basis sets in Gaussian 09 program.[21] The structure of FePz is optimized on both the ground and excited state during calculations. Comparing to the ground state, the positive charge of Fe increases on the excited state, which is consistent regardless of the basis sets, hence confirming the assignment of the MLCT state upon photoexcitation. Therefore, the excited-state FSRS data upon 480 nm photoexcitation (Fig. 2 in main text, Fig. S4 and S5 above) mainly report on an excited iron d-electron configuration with the ground-state porphyrazine ring configuration, wherein ultrafast electron and nuclear motions occur (see main text discussions and TOC Graphic).

ESI References

(1)   Gao, H.; Groves, J. T. Fast Hydrogen Atom Abstraction by a Hydroxo Iron(III) Porphyrazine. *J. Am. Chem. Soc.* **2017**, *139*, 3938-3941.

(2)   Tang, L.; Liu, W.; Wang, Y.; Zhao, Y.; Oscar, B. G.; Campbell, R. E.; Fang, C. Unraveling Ultrafast Photoinduced Proton Transfer Dynamics in a Fluorescent Protein Biosensor for Ca^{2+} Imaging. *Chem. Eur. J.* **2015**, *21*, 6481-6490.

(3)   Liu, W.; Wang, Y.; Tang, L.; Oscar, B. G.; Zhu, L.; Fang, C. Panoramic Portrait of Primary Molecular Events Preceding Excited State Proton Transfer in Water. *Chem. Sci.* **2016**, *7*, 5484-5494.

(4)   Tang, L.; Wang, Y.; Zhu, L.; Lee, C.; Fang, C. Correlated Molecular Structural Motions for Photoprotection After Deep-UV Irradiation. *J. Phys. Chem. Lett.* **2018**, *9*, 2311-2319.

(5)   Tang, L.; Zhu, L.; Taylor, M. A.; Wang, Y.; Remington, S. J.; Fang, C. Excited State Structural Evolution of a GFP Single-Site Mutant Tracked by Tunable Femtosecond-Stimulated Raman Spectroscopy. *Molecules* **2018**, *23*, 2226.

(6)   Tang, L.; Zhu, L.; Wang, Y.; Fang, C. Uncovering the Hidden Excited State toward Fluorescence of an Intracellular pH Indicator. *J. Phys. Chem. Lett.* **2018**, *9*, 4969-4975.

(7)   Zhu, L.; Liu, W.; Fang, C. A Versatile Femtosecond Stimulated Raman Spectroscopy Setup with Tunable Pulses in the Visible to Near Infrared. *Appl. Phys. Lett.* **2014**, *105*, 041106.

(8)   Fang, C.; Frontiera, R. R.; Tran, R.; Mathies, R. A. Mapping GFP Structure Evolution during Proton Transfer with Femtosecond Raman Spectroscopy. *Nature* **2009**, *462*, 200-204.

(9)   Oscar, B. G.; Chen, C.; Liu, W.; Zhu, L.; Fang, C. Dynamic Raman Line Shapes on an Evolving Excited-State Landscape: Insights from Tunable Femtosecond Stimulated Raman Spectroscopy. *J. Phys. Chem. A* **2017**, *121*, 5428-5441.

(10) Fang, C.; Tang, L.; Oscar, B. G.; Chen, C. Capturing Structural Snapshots during Photochemical Reactions with Ultrafast Raman Spectroscopy: From Materials Transformation to Biosensor Responses. *J. Phys. Chem. Lett.* **2018**, *9*, 3253-3263.

(11) Provencher, F.; Bérubé, N.; Parker, A. W.; Greetham, G. M.; Towrie, M.; Hellmann, C.; Côté, M.; Stingelin, N.; Silva, C.; Hayes, S. C. Direct Observation of Ultrafast Long-Range Charge Separation at Polymer-Fullerene Heterojunctions. *Nat. Commun.* **2014**, *5*, 4288.

(12) Bragg, A. E.; Yu, W.; Zhou, J.; Magnanelli, T. Ultrafast Raman Spectroscopy as a Probe of Local Structure and Dynamics in Photoexcited Conjugated Materials. *J. Phys. Chem. Lett.* **2016**, *7*, 3990-4000.

(13) Dietze, D. R.; Mathies, R. A. Femtosecond Stimulated Raman Spectroscopy. *ChemPhysChem* **2016**, *17*, 1224–1251.

(14) Hart, S. M.; Silva, W. R.; Frontiera, R. R. Femtosecond Stimulated Raman Evidence for Charge-Transfer Character in Pentacene Singlet Fission. *Chem. Sci.* **2018**, *9*, 1242-1250.

(15) Ryland, E. S.; Lin, M.-F.; Verkamp, M. A.; Zhang, K.; Benke, K.; Carlson, M.; Vura-Weis, J. Tabletop Femtosecond M-edge X-ray Absorption Near-Edge Structure of FeTPPCl: Metalloporphyrin Photophysics from the Perspective of the Metal. *J. Am. Chem. Soc.* **2018**, *140*, 4691-4696.

(16) Franzen, S.; Kiger, L.; Poyart, C.; Martin, J.-L. Heme Photolysis Occurs by Ultrafast Excited State Metal-to-Ring Charge Transfer. *Biophys. J.* **2001**, *80*, 2372-2385.

(17) Chen, C.; Zhu, L.; Baranov, M. S.; Tang, L.; Baleeva, N. S.; Smirnov, A. Y.; Yampolsky, I. V.; Solntsev, K. M.; Fang, C. Photoinduced Proton Transfer of GFP-Inspired Fluorescent Superphotoacids: Principles and Design. *J. Phys. Chem. B* **2019**, *123*, 3804-3821.

(18) Balakrishnan, G.; Soldatova, A. V.; Reid, P. J.; Spiro, T. G. Ultrafast Charge Transfer in Nickel Phthalocyanine Probed by Femtosecond Raman-Induced Kerr Effect Spectroscopy. *J. Am. Chem. Soc.* **2014**, *136*, 8746-8754.

(19) Fodor, M. A.; Horváth, O.; Fodor, L.; Grampp, G.; Wankmüller, A. Photophysical and Photocatalytic Behavior of Cobalt(III) 5,10,15,20-tetrakis(1-methylpyridinium-4-yl)porphyrin. *Inorg. Chem. Commun.* **2014**, *50*, 110-112.

(20) Chábera, P.; Liu, Y.; Prakash, O.; Thyrhaug, E.; Nahhas, A. E.; Honarfar, A.; Essén, S.; Fredin, L. A.; Harlang, T. C. B.; Kjær, K. S.; et al. A low-spin Fe(iii) complex with 100-ps ligand-to-metal charge transfer photoluminescence. *Nature* **2017**, *543*, 695-699.

(21) Frisch, M. J.; Trucks, G. W.; Schlegel, H. B.; Scuseria, G. E.; Robb, M. A.; Cheeseman, J. R.; Scalmani, G.; Barone, V.; Mennucci, B.; Petersson, G. A.; et al. *Gaussian 09, Revision B.1*; Gaussian, Inc.: Wallingford, CT, 2009.

(22) Scott, A. P.; Radom, L. Harmonic Vibrational Frequencies: An Evaluation of Hartree−Fock, Møller−Plesset, Quadratic Configuration Interaction, Density Functional Theory, and Semiempirical Scale Factors. *J. Phys. Chem.* **1996**, *100*, 16502-16513.

(23) Baerends, E. J.; Ricciardi, G.; Rosa, A.; van Gisbergen, S. J. A. A DFT/TDDFT Interpretation of the Ground and Excited States of Porphyrin and Porphyrazine Complexes. *Coord. Chem. Rev.* **2002**, *230*, 5-27.

(24) Ashley, D. C.; Jakubikova, E. Ironing Out the Photochemical and Spin-Crossover Behavior of Fe(II) Coordination Compounds with Computational Chemistry. *Coord. Chem. Rev.* **2017**, *337*, 97-111.

Full Authorship for the *Gaussian 09* (Revision B.1) software:

Frisch, M. J.; Trucks, G. W.; Schlegel, H. B.; Scuseria, G. E.; Robb, M. A.; Cheeseman, J. R.; Scalmani, G.; Barone, V.; Mennucci, B.; Petersson, G. A.; Nakatsuji, H.; Caricato, M.; Li, X.; Hratchian, H. P.; Izmaylov, A. F.; Bloino, J.; Zheng, G.; Sonnenberg, J. L.; Hada, M.; Ehara, M.; Toyota, K.; Fukuda, R.; Hasegawa, J.; Ishida, M.; Nakajima, T.; Honda, Y.; Kitao, O.; Nakai, H.; Vreven, T.; J. A. Montgomery, J.; Peralta, J. E.; Ogliaro, F.; Bearpark, M.; Heyd, J. J.; Brothers, E.; Kudin, K. N.; Staroverov, V. N.; Kobayashi, R.; Normand, J.; Raghavachari, K.; Rendell, A.; Burant, J. C.; Iyengar, S. S.; Tomasi, J.; Cossi, M.; Rega, N.; Millam, J. M.; Klene, M.; Knox, J. E.; Cross, J. B.; Bakken, V.; Adamo, C.; Jaramillo, J.; Gomperts, R.; Stratmann, R. E.; Yazyev, O.; Austin, A. J.; Cammi, R.; Pomelli, C.; Ochterski, J. W.; Martin, R. L.; Morokuma, K.; Zakrzewski, V. G.; Voth, G. A.; Salvador, P.; Dannenberg, J. J.; Dapprich, S.; Daniels, A. D.; Farkas, Ö.; Foresman, J. B.; Ortiz, J. V.; Cioslowski, J.; Fox, D. J.